1-25-2018

Carbon Nanofibers (CNFs) Supported Cobalt-Nickel Sulfide (CoNi 2 S 4) Nanoparticles Hybrid Anode for High Performance Lithium Ion Capacitor

Ajay Jagadale

Xuan Joe Zhou

Douglas Blaisdell

Sen Yang

SCIENTIFIC REPORTS

OPEN

Carbon nanofibers (CNFs) supported cobalt- nickel sulfide (CoNi$_2$S$_4$) nanoparticles hybrid anode for high performance lithium ion capacitor

Ajay Jagadale[1], Xuan Zhou[1], Douglas Blaisdell[1] & Sen Yang[2]

Lithium ion capacitors possess an ability to bridge the gap between lithium ion battery and supercapacitor. The main concern of fabricating lithium ion capacitors is poor rate capability and cyclic stability of the anode material which uses sluggish faradaic reactions to store an electric charge. Herein, we have fabricated high performance hybrid anode material based on carbon nanofibers (CNFs) and cobalt-nickel sulfide (CoNi$_2$S$_4$) nanoparticles via simple electrospinning and electrodeposition methods. Porous and high conducting CNF@CoNi$_2$S$_4$ electrode acts as an expressway network for electronic and ionic diffusion during charging-discharging processes. The effect of anode to cathode mass ratio on the performance has been studied by fabricating lithium ion capacitors with different mass ratios. The surface controlled contribution of CNF@CoNi$_2$S$_4$ electrode was 73% which demonstrates its excellent rate capability. Lithium ion capacitor fabricated with CNF@CoNi$_2$S$_4$ to AC mass ratio of 1:2.6 showed excellent energy density of 85.4 Wh kg^{-1} with the power density of 150 W kg^{-1}. Also, even at the high power density of 15 kW kg^{-1}, the cell provided the energy density of 35 Wh kg^{-1}. This work offers a new strategy for designing high-performance hybrid anode with the combination of simple and cost effective approaches.

High energy density, high power density and long cycle life are the main requirements of future energy storage devices in order to use them in different moderns applications such as consumer electronic devices, hybrid electric vehicles and large scale grid energy storage[1]. In the last two decades, number of research articles have been published in the field of energy storage devices which are mainly focusing on the supercapacitors (SCs) and lithium ion batteries (LIBs). SCs store an electrical energy via non-faradaic process which includes adsorption/desorption of electrolytic charges on the surface of electrode materials. However, LIBs use intercalation/deintercalation of lithium ions in the host materials. Due to their electric double layer type (EDL) charge storage mechanism, SCs provide high power density ($>$10 kW kg^{-1}) and good cyclic life ($>$10^5 cycles), however, due to the limited accumulation of charges they exhibit lower energy performance ($<$10 Wh kg^{-1}). Besides, LIBs deliver high energy performance (150–200 Wh kg^{-1}) due to diffusion controlled slow faradaic reactions throughout the active material. In the present state of art, these two devices are inadequate to be used for many applications such as electric vehicles and plugged in electric vehicles.

Recently, Lithium ion capacitors (LICs) have attracted great attention because of their extraordinary electrochemical properties. LICs bridge the gap between SCs and LIBs by combining merits of both systems[2]. Basically, LICs are made up of high energy LIB anode, high power SC cathode and Li ion containing organic electrolyte (mainly LIB electrolyte). In 2001, Amatucci et al.[3] first fabricated LIC at the Telcordia technologies using nanostructured Li$_4$Ti$_5$O$_{12}$ (LTO) anode, activated carbon (AC) cathode and Li$^+$ ion containing organic electrolyte. Till date, many research articles have been published which are mainly focused on the novel anode and cathode

[1]Department of Electrical and Computer Engineering, Kettering University, Flint, MI-48504, USA. [2]School of Science, MOE Key Laboratory for Nonequilibrium Synthesis and Modulation of Condensed Matter, Xi'an Jiaotong University, Xi'an, 710049, China. Correspondence and requests for materials should be addressed to X.Z. (email: xzhou@kettering.edu)
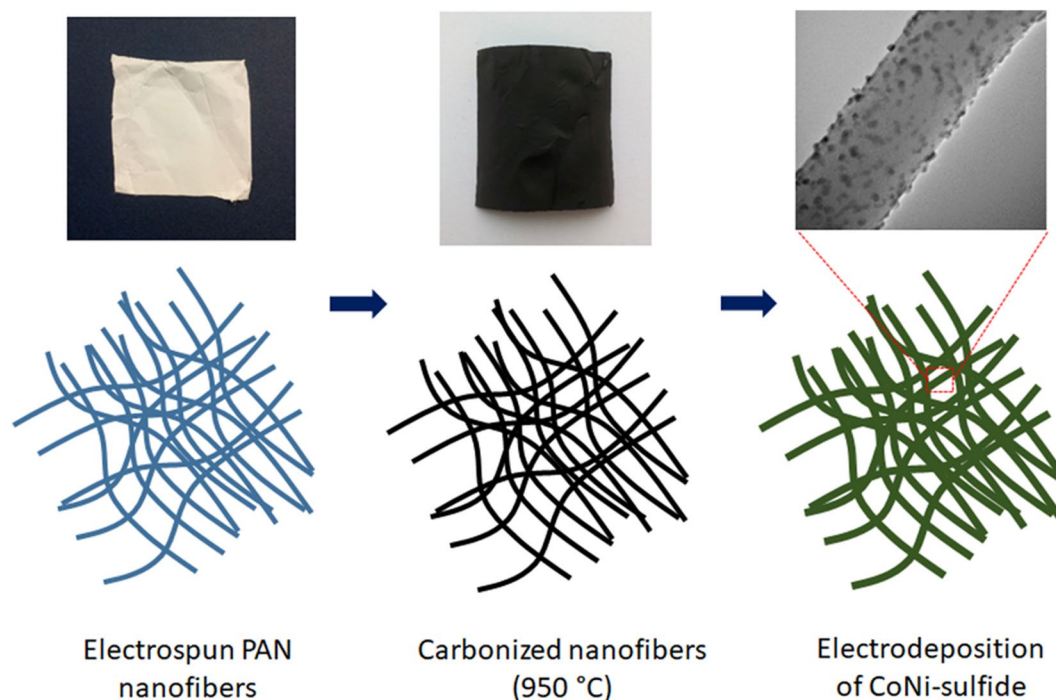
Figure 1. schematics of the formation process of CNF@CoNi$_2$S$_4$ electrode.

materials. Generally, Li$^+$ insertion based anode provides high energy density to the LIC, however, due to the sluggish kinetics, it results into poor power performance. In order to improve both power and energy densities simultaneously, preparation of nanostructured and high electrical conductivity anodes are desirable. Previously, research in the anode materials have been focused on the development of hybrid electrodes by applying conductive carbon coating and preparing controlled nanostructured morphology. Carbon coating on the active material surface provides fast electronic diffusion which leads to the increased rate capability and high power performance. The nanostructured morphology offer reduced pathways for ionic and electronic diffusion and enhanced surface activity for charge storage. Previously, different anode materials have been reported such as LTO[4], graphite[5], graphdiyne[6], Si[7], Mn$_3$O$_4$-graphene[8], TiO$_2$[9], graphene[10], LiTi$_{1.5}$Zr$_{0.5}$(PO$_4$)$_3$[11], soft carbon[12], NbN[13], LiMnBO$_3$[14], SnO$_2$-C[15], hard carbon[16], Nb$_2$O$_5$@graphene[17], TiO$_2$-B[18], etc. Cathodes such as AC, Nb$_2$CT$_x$-carbon nanotube[19], graphene[20], carbide-derived carbon[21] have been mostly reported. In the aforementioned materials, binders and conductive additives are preferably used. However, these components increase the dead mass of the electrode that makes an obstacle for ionic diffusion in the active material which further deteriorates the cell performance. Also, anodes like LTO, TiO$_2$ and Nb$_2$O$_5$ possess poor electrical conductivity that restricts them to be efficiently utilized in LIC. In this scenario, preparation of self-standing binder-free high conductivity electrodes is highly anticipated.

Recently, transition metal sulfide (TMS) anodes have attracted great attention because of their superior capacity values as compared to the conventional graphite (372 mAh g^{-1}) and LTO (170 mAh g^{-1}) anodes. Also, the high electrical conductivity of TMSs facilitates pathways for electron transportation which lead to the high power performance. Recently, very few sulfides have been utilized as an anode in LIC, for example, Zhang *et al.*[22] fabricated MoS$_2$ incorporated onto 3D porous graphene and Amaresh *et al.*[23] used cubic CoS$_2$ nanoparticles as anodes for LIC. Apart from this, different TMSs have been frequently reported as anodes in LIBs including WS$_2$[24], MoS$_2$[25], Cu$_2$S[26], Ni$_3$S$_4$ and NiS$_{1.03}$[27], SnS$_2$[28], CoS[29], Bi$_2$S$_3$[30], NiCo$_2$S$_4$[31], etc. Among the available sulfide anodes, mixed metal sulfides, for example, NiCo$_2$S$_4$ and CoNi$_2$S$_4$ have great importance due to their excellent electrical conductivity, high redox activity and high theoretical capacity around 703 mAh g^{-1}.

On the other hand, carbon matrix, especially carbon nanofibers can enhance the electrical conductivity of the electrode and endure the stresses occurred during cycling[32,33]. By considering above facts, in the present investigation, we have prepared carbon nanofibers (CNF) using electrospinning method and used as a scaffold for the electrodeposition of cobalt nickel sulfide (CoNi$_2$S$_4$) nanoparticles. This nanoparticle coated carbon nanofiber hybrid webs provide high surface area and open channels for efficient electron/ion transport which leads to the superior electrochemical performance. Furthermore, LICs were prepared by using CNF@CoNi$_2$S$_4$ as an anode and activated carbon as a cathode. AC//CNF@CoNi$_2$S$_4$ LIC fabricated with anode to cathode mass ratio of 1:2.6 delivered energy density of 85.4 Wh kg^{-1} with the power density of 150 W kg^{-1} and showed excellent cyclic stability of 96% after 5000 cycles.

Results and Discussion

Figure 1 shows schematic of formation process of CNF@CoNi$_2$S$_4$ anode which involves three steps. In the first step, PAN nanofibers were prepared using electrospinning method. Furthermore, as synthesized PAN nanofibers
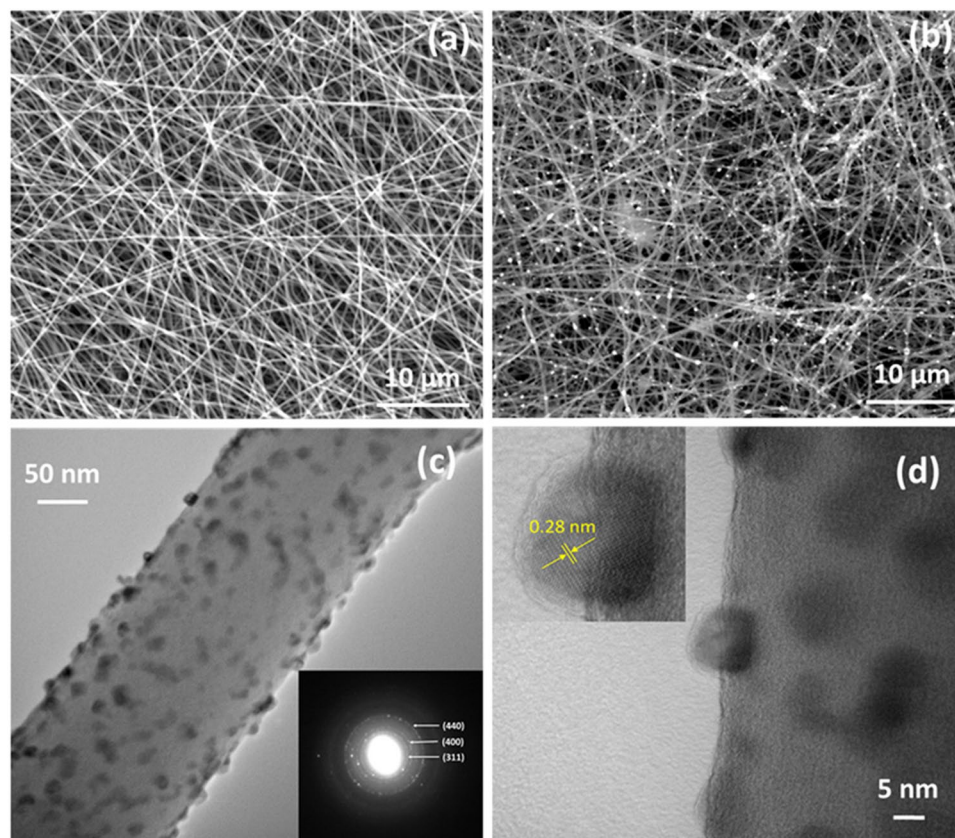
Figure 2. E-SEM images of (**a**) bare CNFs, (**b**) CNFs loaded with CoNi$_2$S$_4$ nanoparticles, (**c**) TEM image of single CNF decorated with CoNi$_2$S$_4$ nanoparticles (Inset: SAED pattern), and (**d**) high resolution-TEM image of CoNi$_2$S$_4$ nanoparticle supported on CNF (Inset: lattice spacing corresponds to 311 plane of single CoNi$_2$S$_4$ nanoparticle).

were stabilized and carbonized. Finally, carbonized nanofibers were used as a substrate for the deposition of Co-Ni sulfides. As shown in the figure, CoNi$_2$S$_4$ nanoparticles were homogeneously deposited on the surface of CNF.

Morphology of the CNF@CoNi$_2$S$_4$ is investigated by E-SEM and TEM. Figure 2a,b show E-SEM images of bare CNFs and CNFs loaded with CoNi$_2$S$_4$ samples. From the figure, it is seen that the bare carbon nanofibers construct 3D porous structure with randomly dispersed smooth fibers of the diameter of 200 to 300 nm. As shown in the Fig. 2b, CoNi$_2$S$_4$ particles are formed on the surface of CNFs, however, these are microsized larger particles. In the electrodeposition method, particles start growing at electrochemically active sites, some particles grow faster than normal because of inhomogeneous distribution of surface activity. In order to visualize the very surface of the CNF, TEM has been used. Figure 2c shows TEM image of the CNF@CoNi$_2$S$_4$ sample which confirms the formation of CoNi$_2$S$_4$ nanoparticles on the surface of CNF with the diameter of 10 to 15 nm. The SAED pattern depicts the polycrystalline nature of CoNi$_2$S$_4$ by indexing planes as (311), (400) and (440) (Inset of Fig. 2c). Figure 2d shows high resolution TEM image of the CoNi$_2$S$_4$ particles which depicts that the nanoparticles are firmly attached to the surface of CNF (inset of Fig. 2d). Interestingly, it seems that the particles are hard to be detached since there were no particles observed in the background of TEM images. Also, the inset of the Fig. 2d shows that the lattice spacing of 0.28 nm corresponds to the 311 crystal planes of CoNi$_2$S$_4$ which is consistent with XRD results. Recently, similar structure has been reported by Li *et al.*[34] by fabricating Co$_3$O$_4$ nanoparticles-decorated carbon nanofibers as an air-cathode for rechargeable Zn-air batteries. In another study, Shen *et al.*[35] have loaded Tin nanoparticles on the carbon nanofibers for their application as an anode in LIBs.

Figure 3a shows XRD pattern of CNF@CoNi$_2$S$_4$ sample which represents diffraction peaks at 2θ of 26.3, 31.2, 37.8, 50.0 and 54.8° can be indexed to (220), (311), (400), (511) and (440) planes of cubic CoNi$_2$S$_4$ (JCPDS card no. 24–0334). Peaks from the carbon nanofibers are not observed due to their amorphous nature. Also, the average crystallite size of CoNi$_2$S$_4$ was estimated as 25.7 nm on the basis of full width at half maxima intensity of XRD peak for (311) plane using Scherrer's formula,

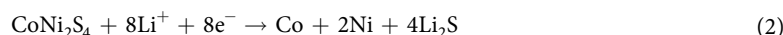$$D = \frac{0.89\lambda}{\beta \cos\theta} \tag{1}$$

where 'D' is average crystallite size, 'β' is full width at half maxima, 'λ' is wavelength of X-ray used and 'θ' is diffraction angle. This size is reasonably comparable with the size observed with high resolution TEM image. This
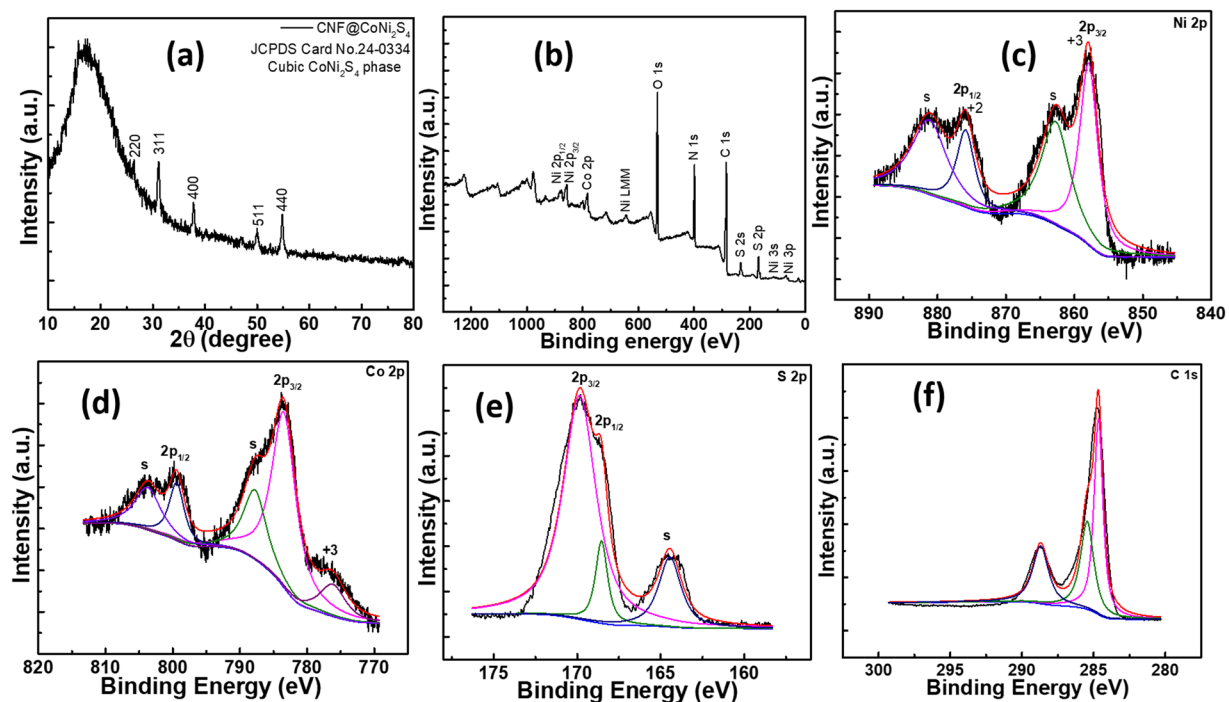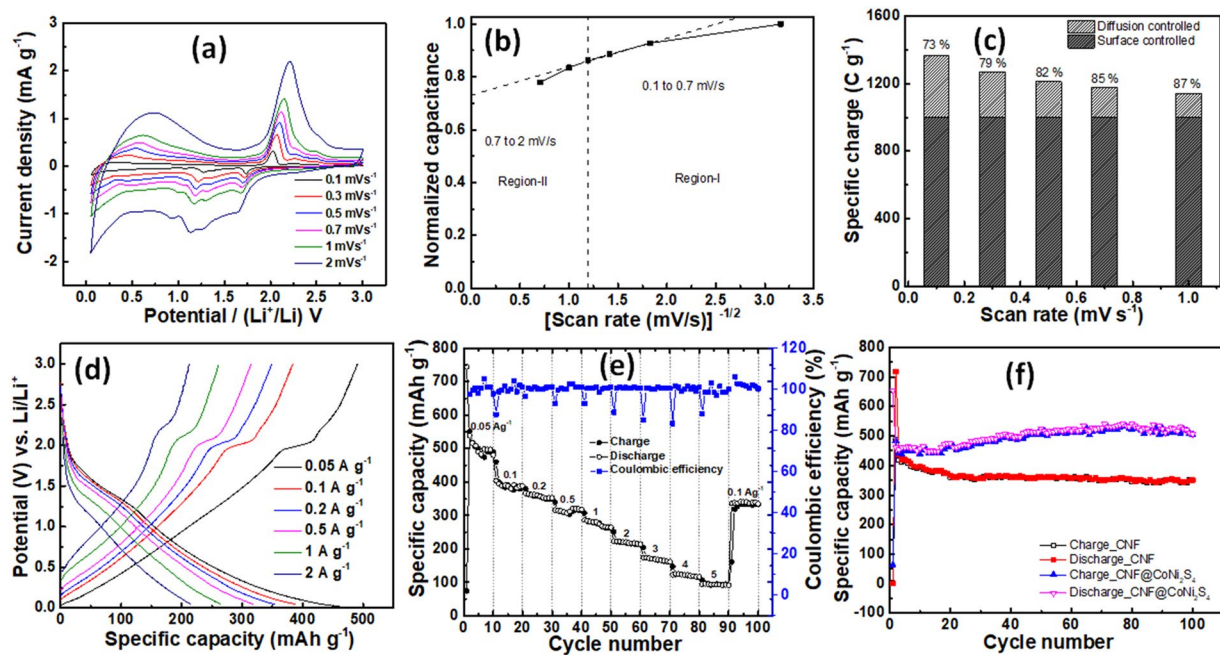
Figure 3. (**a**) XRD pattern, (**b**) XPS survey, (**c**) Ni 2p, (**d**) Co 2p, (**e**) S 2p, and (**f**) C 1 s spectra of CNF@CoNi$_2$S$_4$ sample.

XRD data is quite consistent with the literature[35,36]. Furthermore, the XPS measurements were carried out in order to understand the surface electronic states of the CNF@CoNi$_2$S$_4$ sample. Figure 3b shows the survey spectrum recorded for CNF@CoNi$_2$S$_4$ sample which demonstrates the presence of Ni, Co, S and C elements. The high resolution spectrum of Ni 2p is fitted with two shakeup satellites (s) by using a Gaussian fitting method. As shown in the Fig. 3c, two strong peaks centered at binding energies of 857.8 and 875.8 eV are attributed to Ni^{3+} and Ni^{2+} ions[37]. The satellite peaks at around 862.7 and 881.1 eV are two shakeup type peaks of Ni at the upper binding energy sides of Ni 2p$_{3/2}$ and Ni 2p$_{1/2}$, respectively[38]. Figure 3d shows the Co 2p spectrum, the binding energy centered at 776.2 eV of the Co 2p peak are assigned to Co^{3+} and the binding energies at 783.4 and 799.4 eV to Co^{2+}. The existence of Co 2p$_{3/2}$ and Co 2p$_{1/2}$ peaks indicates the presence of both Co^{3+} and Co^{2+} ions[39]. As shown in Fig. 3e, the S 2p spectrum depicts two peaks with the binding energies centered at 169.8 and 164.4 eV which correspond to the main and shakeup satellite peaks, respectively. The second satellite peak designates the bonding between metal and sulfur, in the present case, Ni-S and Co-S bondings[37]. As the CNF@CoNi$_2$S$_4$ electrode was mainly formed of carbon, it was desirable to understand the electronic states of the carbon. Figure 3f shows the C1s spectrum comprised of three different peaks centered at 284.6, 285.4 and 288.6 eV which might be attributed to the single and double bonds between carbon (C-C, C=C), carbon interacted with hydroxyl and epoxy groups (C-OH, C-O-C), and carboxylic groups (COO), respectively[40]. This result confirms the formation of CoNi$_2$S$_4$ on the surface of CNF and also supports the data obtained by XRD study.

Figure S1 (supporting information) shows 1st, 2nd, and 3rd CV curves of CNF@CoNi$_2$S$_4$, 1st CV cycle depicts three distinct cathodic peaks at 1.7, 1.2 and 0.7 V which can be assigned to the reduction of Co^{2+} and Ni^{3+} into metallic Co and Ni, respectively. Also, peaks observed at around 2.0, 2.2 and 2.4 V in the subsequent anodic scan can be attributed to the oxidation of metallic Ni and Co to NiS$_x$ and CoS$_x$, respectively[31,41]. In the 2nd and 3rd cycles, the main cathodic peaks shifted toward a higher potential and the anodic peaks shifted slightly toward lower potential. This shifting and decrease in the cathodic peak currents might be due to the existence of certain irreversible reactions associated with the formation of a solid electrolyte interphase (SEI) film on the electrode surface[42]. Furthermore, the overlapping of 2nd and 3rd CV curves indicates an excellent reversibility of the CNF@CoNi$_2$S$_4$ electrode. The redox reversibility of the CNF@CoNi$_2$S$_4$ electrode has been evaluated using Laviron's theory with the calculation of heterogeneous electron transfer rate constant using Kochi's method (supporting information, S1). The electrochemical reaction associated with the charging-discharging process of the CNF@CoNi$_2$S$_4$ electrode can be illustrated as follows[41,43],

$$CoNi_2S_4 + 8Li^+ + 8e^- \rightarrow Co + 2Ni + 4Li_2S \tag{2}$$

$$Co + Li_2S \leftrightarrow CoS + 2Li^+ + 2e^- \tag{3}$$

$$Ni + Li_2S \leftrightarrow NiS + 2Li^+ + 2e^- \tag{4}$$

Figure 4. (**a**) CV curves of CNF@CoNi$_2$S$_4$ electrode at different scan rates range from 0.1 to 2 mV s^{-1}, (**b**) variation of normalized capacitance and [scan rate (mV s^{-1})]$^{-1/2}$, (**c**) surface and diffusion controlled charge storage contributions at different scan rates for CNF@CoNi$_2$S$_4$ electrode, (**d**) GCD curves of of CNF@CoNi$_2$S$_4$ electrode at different current densities range from 0.05–2 A g^{-1}, (**e**) rate perfromance of CNF@CoNi$_2$S$_4$ at current densities of 0.05, 0.1, 0.2, 0.5, 1, 2, 3, 4, 5 A g^{-1}, and (**f**) cyclic performance of CNF@CoNi$_2$S$_4$ and CNF at the current density of 0.1 A g^{-1}.

$$CoS + 1/3Li_2S \leftrightarrow 1/3Co_3S_4 + 2/3Li^+ + 2/3e^- \qquad (5)$$
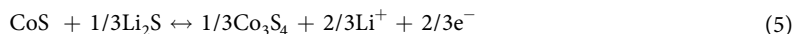
In order to investigate the electrochemical performance of CNF@CoNi$_2$S$_4$ electrode, CV measurements were carried out at various scan rates ranging from 0.1 to 2 mV s^{-1} (Fig. 4a). As shown from CV curves, when the scan rate increased, area under the curve also increased which is in accordance with the high rate capability of the CNF@CoNi$_2$S$_4$ electrode. Also, Fig. S3 (supporting information) shows the variation of specific charge and scan rate. The capacity retention of 78% at relatively highest scan rate (2 mV s^{-1}) demonstrates high rate capability of the CNF@CoNi$_2$S$_4$ electrode. Furthermore, it is necessary to ensure the quantitative analysis of charge storage contributions in the anode materials, recently, Trasatti procedure has attracted great attention because of its ability to distinguish different charge storage contributions in the anode materials[44–46]. According to the Trasatti procedure, the total charge storage (q*) involves both outer (q$_o$) and inner (q$_i$) charge storage, this can be seen by the equation below,

$$q_* = q_0 + q_i \qquad (6)$$

The outer charge is mainly originated due to the surface capacitive reactions and the inner charge due to the diffusion controlled insertion reaction. Therefore, specific charge storage at various scan rates can be estimated by using equation,

$$q = q_\infty + k/v^{1/2} \qquad (7)$$

where v and k are scan rate and constant, respectively. Figure 4b shows the plot of normalized capacitance versus inverse of root of scan rate ($v^{-1/2}$) for CNF@CoNi$_2$S$_4$ from a scan rate of 0.1–2 mV s^{-1}. The plot distinguishes into two regions, the region-I (0.1–0.7 mV s^{-1}) and the region –II (0.7–2 mV s^{-1}). In the region-I, the normalized capacitance was seen to be independent or inadequately dependent on the scan rate, however, in the region-II, normalized capacitance started to decrease quickly when the scan rate increased. The capacitive or the surface controlled contribution can be estimated by extrapolated y-intercept which was found to be 73%. Here, it is worth mentioning that the remaining only 27% contribution was originated from the diffusion controlled kinetics. In order to prepare excellent anode materials for LIC, it is desirable to use electrode with greater capacitive or surface-controlled contributions. This kind of electrodes can facilitate excellent rate capability or the power capability without compromising energy performance. Recently, the capacitive contributions for 3D interconnected TiC and 2D nanosheets structured ZnMn$_2$O$_4$-graphene have been reported as 78% (0.5 mV s^{-1}) and 24.2% (0.2 mV s^{-1}), respectively[47,48]. An excellent capacitive contribution in the present case might be attributed to the excellent rate capability of the electrode which can be originated due to the high conductivity and open porous structure of the CNF@CoNi$_2$S$_4$ electrode. Furthermore, as shown in the Fig. 4c, when the scan rate increased
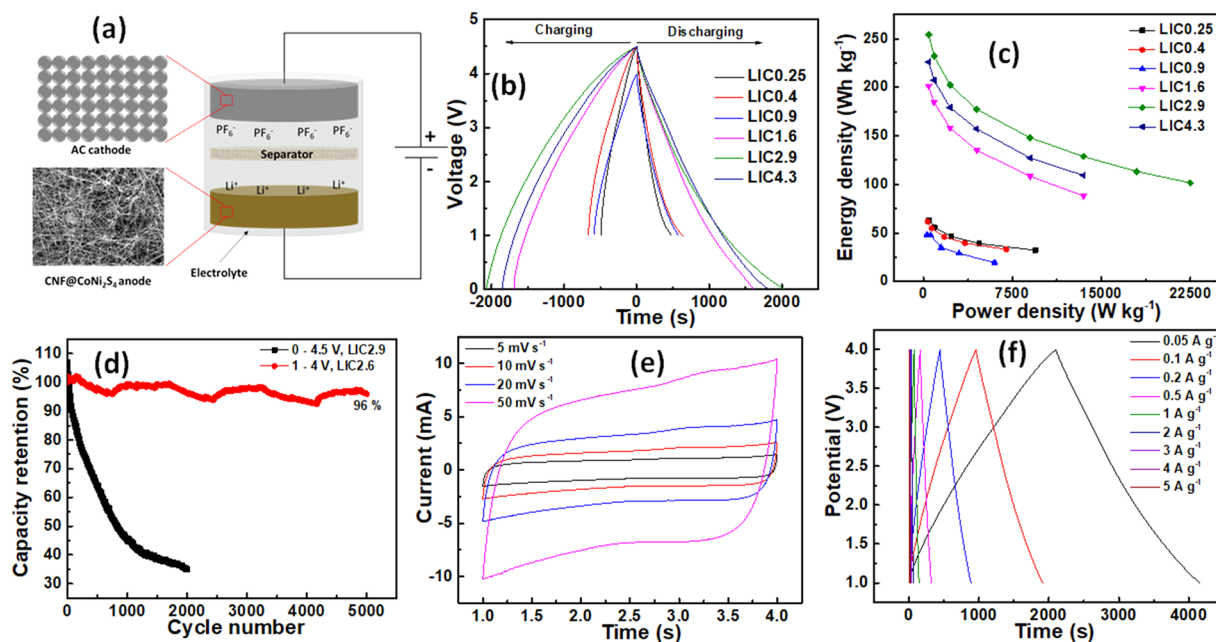
Figure 5. (**a**) Schematic of the LIC based on AC cathode and CNF@CoNi$_2$S$_4$ anode, (**b**) GCD curves of LICs fabricated with different anode to cathode mass ratios at constant current density of 0.1 A g^{-1}, (**c**) Ragone plot with values of energy and power densities for different LICs, (**d**) cyclic performance of LIC2.6 (1–4 V) and LIC2.9 (0–4.5 V) at the current density of 2 A g^{-1}, (**e**) CV curves of LIC2.6 at different scan rates range from 5–50 mV s^{-1}, and (**f**) GCD curves of LIC2.6 at different current densities range from 0.05–5 A g^{-1}.

from 0.1 to 1 mV s^{-1}, the diffusion controlled contribution decreased which can be attributed to the diffusion limitations and increased ohmic contribution[48].

The rate capability was examined by recording galvanostatic charging discharging (GCD) curves of the CNF@CoNi$_2$S$_4$ electrode at various current densities ranging from 0.05–2 A g^{-1}. Figure 4d shows the GCD curves at various current densities performed within the potential window of 0.005–3 V vs. (Li$^+$/Li), which depicts the excellent coulombic efficiency of 100%. As shown in the Fig. 4e, CNF@CoNi$_2$S$_4$ was able to deliver a specific capacity of 497 mAh g^{-1} at 0.05 A g^{-1} (10th cycle), which is far greater than the theoretical capacities of graphite and LTO[21]. Also, when the current density increased by 10 folds to 0.5 A g^{-1}, the specific capacity was found to be 319 mAh g^{-1}. The rate capability in the present case is quite comparable with that of obtained for carbon paper supported CoNi$_2$S$_4$ nanorods arrays[49]. This is because, good conducting, porous and high surface area CNFs facilitate fast and efficient ionic and electronic diffusion during charging discharging process. Furthermore, after the rigorous cycling at higher current density of 10 A g^{-1}, the specific capacity at the 0.1 A g^{-1} was recovered back close to initial cycling capacity, which certainly proves the superior rate capability of the CNF@CoNi$_2$S$_4$ electrode.

Furthermore, in order to understand the cyclic performance of the CNF@CoNi$_2$S$_4$ electrode, the charge-discharge cycling was performed at the current density of 0.1 Ag^{-1} for 100 cycles and compared with the bare CNF (Fig. 4f). During cycling, the capacity of the CNF@CoNi$_2$S$_4$ increased up to certain extent and appeared to be stabilized. However, the capacity of the bare carbon nanofibers was decreased during the first couple of cycles and stabilized. The capacity increment in case of CNF@CoNi$_2$S$_4$ can be attributed to the electrochemical activation of the electrode[50]. An excellent electrochemical performance in terms of specific capacity, rate capability and cyclic stability of the CNF@CoNi$_2$S$_4$ electrode can be attributed to the following points. 1) Well-distributed nanoparticles of the CoNi$_2$S$_4$ on the CNF surface facilitate enhanced surface area for the electrochemical charge storage, besides, the extra spacing between two adjacent particles offers extra space for the expansion of the particles during lithiation process which improves cyclic performance. Also, as discussed in the TEM results, these particles are strongly attached to the CNF which also empowers the cyclic life of the particle-derived nanocomposite electrodes. 2) The structure of CNF@CoNi$_2$S$_4$ electrode is mainly comprised of CNF webs and CoNi$_2$S$_4$ nanoparticles which is highly porous structure that offers reduced pathways for electrolytic diffusion, moreover, the good conducting behavior of both CoNi$_2$S$_4$ and CNF acts as an expressway for electronic diffusion through the electrode network, this enhances the rate capability of the electrode. 3) Carbon matrix near the interface of nanoparticle and the CNF accommodates the expansion of the CoNi$_2$S$_4$ and prevents the pulverization of nanoparticles which further improves cyclic life of the electrode.

As shown in the Fig. 5a, LICs were fabricated using AC as a cathode and prelithiated CNF@CoNi$_2$S$_4$ as an anode in 1 M LiPF$_6$ in EC-DEC electrolyte solution. Before fabrication of the LICs, CNF@CoNi$_2$S$_4$ electrodes were first prelithiated by directly contacting with lithium foil with one or two drops of electrolyte. The charge storage mechanism of the LIC is based on both faradaic and non-faradaic electrochemical reactions. During charging process, Li$^+$ ions from the electrolyte are intercalated into the CNF@CoNi$_2$S$_4$ nanocomposite material, while PF$_6^-$ ions are adsorbed on the high surface area AC cathode. In order to utilize full benefits of CNF@CoNi$_2$S$_4$ electrode,

it is necessary to balance charges on both electrodes. In the present investigation, different LICs were fabricated with anode to cathode mass ratios of 1:0.25, 1:0.4, 1:0.9, 1:1.6, 1:2.9 and 1:4.3, and respectively labeled as LIC0.25, LIC0.4, LIC0.9, LIC1.6, LIC2.9 and LIC4.3. Furthermore, the electrochemical performance of the LICs was examined using cyclic voltammetry, GCD and EIS. Figure 5b shows the GCD curves of LICs fabricated with different anode to cathode ratios at 0.1 A g^{-1}. Interestingly, the GCD curves are slightly deviated from the ideal triangular shape which might be due to the combination of both faradaic and non-faradaic reactions involved during charging-discharging processes. Also, GCD curves are symmetric in nature which suggests its high reversibility and excellent coulombic efficiency. The operating potential window of the each LIC was optimized and found to be 1 to 4.5 V (LIC0.25 and LIC0.4), 1 to 4 V (LIC0.9) and 0 to 4.5 V (LIC1.6, LIC2.9 and LIC4.3). The capacitance (C_{cell}) of the cell was calculated using equation $C_{cell} = i \times t/\Delta V$, where i is the discharging current (A), t is the discharging time (s) and ΔV is a difference between upper and lower potentials of the discharging curve (V). Further, the specific capacitance (C_{SP}) of the cell was calculated based on the total mass of both electrodes by using a formula $C_{SP} = 4C_{cell}/m$, where m is the total mass (g). The maximum specific capacitances (at 0.1 A g^{-1}) were obtained as 74, 72, 77, 143, 181 and 161 F g^{-1} for LIC0.25, LIC0.4, LIC0.9, LIC1.6, LIC2.9 and LIC4.3, respectively.

Furthermore, the energy and power densities of the LICs were calculated using formulae given in the experimental section. Figure S3 shows GCD curves for all LICs at different current densities (supporting information). Figure 5c shows Ragone plots composed of values of energy and power densities for LICs fabricated with different anode to cathode ratios. It is worth noting that the energy and power densities of LIC fabricated with anode to cathode mass ratio of 1:2.9 found to be phenomenally high as 254 Wh kg^{-1} at the power rating of 450 W kg^{-1}. Also, the same LIC can facilitate the maximum power density of 22.5 kW kg^{-1} with energy density of 101 Wh kg^{-1}. These values of energy and power densities are still beyond the limit of supercapacitor and LIB, respectively. Interestingly, the LICs with lower mass ratios showed poor values of energy and power densities which might be attributed to the imbalanced charge storage on both electrodes which minimizes an operating potential window of the cell. Further, when the mass ratio increased, the energy and power densities were also increased up to certain extent, however, when the mass ratio increased around 1:4.3, the energy and power densities were decreased because of the increased inactive or dead masses in the cathode material. Furthermore, due to the excellent capacitive performance of LIC2.9, it was employed for the cyclic stability study by GCD cycling for 2000 cycles at 2 A g^{-1} within potential window of 0.005–4.5 V. As shown in the Fig. 5d, the capacity of the LIC2.9 was surprising decreased which might be due to the large potential window that causes decomposition of electrolyte and deprivation of cycling stability. In order to confirm the interpretation on the capacity loss, we fabricated the new LIC with approximately similar anode to cathode mass ratio of 1:2.6 (LIC2.6) and employed for stability study at current density of 2 A g^{-1} within a reduced potential window of 1–4 V. The stability performance of LIC2.6 has been showed in the Fig. 5d which demonstrated the huge capacity retention of 96% after 5000 cycles. Figure 5e shows the cyclic voltammetry curves recorded for the LIC2.6 at different scan rates ranging from 5–50 mV s^{-1}. The curves are rather deviated from the ideal rectangular shape which can be attributed to the combination of both faradaic and non-faradaic electrochemical processes on both electrodes. Also, when the scan rate increased, the area under the curves also increased which is in good agreement with ideal supercapacitive behavior, also it confirms that the electrochemical reactions are surface controlled rather than diffusion controlled. Figure 5f shows the GCD curve of LIC2.6 at different current densities varied from 0.05–5 A g^{-1} within a potential window of 1–4 V. GCD curves are triangular with little bit of deviation from the ideal triangular shape which is consistent with the cyclic voltammetry study (Fig. 5e). The values of specific capacitance were found to be 137, 127, 118, 106, 95, 82, 71, 63 and 56 F g^{-1} at the current densities of 0.05, 0.1, 0.2, 0.5, 1, 2, 3, 4 and 5 A g^{-1}, respectively. When the current density increased by 100 folds to 5 A g^{-1}, the value of the specific capacitance still maintained up to 41% which demonstrates the superior rate capability of the LIC2.6.

Figure 6a shows the Ragone plot for LIC2.6 obtained by the calculation of energy and power densities from the GCD curves. LIC2.6 showed the maximum energy density of the 85.4 Wh kg^{-1} with the power delivery of 150 W kg^{-1} at the current density of 0.05 A g^{-1}. Interestingly, even at the high power density of 15 kW kg^{-1}, LIC2.6 still can maintain the energy density of 35 Wh kg^{-1}. These values of energy and power densities in the present case are quite comparable with the literature[51–61].

In order to understand the effect of cycling on the resistive behavior of the LIC, LIC2.6 was employed for EIS analysis. Figure 6b shows Nyquist plots of LIC2.6 obtained before cycling and after 5000 cycles (2 A g^{-1}) within a frequency range from 0.1 Hz to 100 kHz for an applied AC amplitude of 5 mV at the open circuit potential. As shown in the Nyquist plot, two semicircles are observed at high to mid-frequency region with inclined line at low frequency region, however, second semicircle is not distinct in the plot of before cycling. The equivalent circuit model fitted for the impedance data is shown in the inset of Fig. 6b and the calculated data is plotted as a line plots. The equivalent circuit exhibits elements such as R$_s$, R$_{sf}$, R$_{ct}$, CPE and W$_1$ which correspond to the solution resistance, lithium ion migration resistance through the SEI (solid electrolyte interphase) layer[62], charge transfer resistance, constant phase element and Warburg impedance, respectively. An intercept to the real Z axis designates as the solution resistance Rs which can be caused due to the ionic resistance of Celgard separator, electrical resistance of both AC and CNF@CoNi$_2$S$_4$ and contact resistances between active materials and current collectors. In the present case, R$_s$ was estimated to be 2.6 and 3.5 Ω for before cycling and after cycling, respectively. It is seen that the internal resistance of the cell doesn't change significantly. The first semicircle in the high to mid-frequency region can be recognized as the SEI film resistance which might be formed on the negative electrode of the LIC and the values were found to be 3.3 and 9.7 Ω for before and after cycling. Interestingly, after cycling, the SEI film resistance increased which can be attributed to the increased thickness of the SEI layer over cycling[63]. The second semicircle in the mid-frequency region represents the charge transfer resistance which was estimated to be 9 and 24.8 Ω for before and after cycling, respectively. The increased value of the R$_{ct}$ is ascribed to
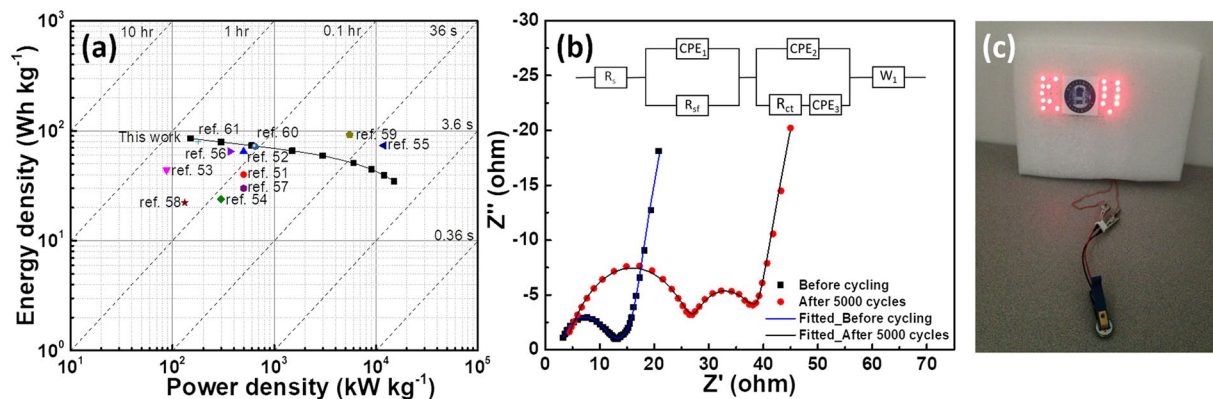
Figure 6. (**a**) Ragone plot of LIC2.6 with scattered points designate the data of LICs taken from the literature, (**b**) Nyquist plots of LIC2.6 before and after cycling within a frequency range from 0.1 Hz to 100 kHz at the open circuit potential (Inset: equivalent circuit fitted for the impedance data), and (**c**) A demonstration of 18 LEDs lighted by the AC//CNF@CoNi$_2$S$_4$ LIC.

Sample	R$_s$ (Ω)	R$_{sf}$ (Ω)	R$_{ct}$ (Ω)	C (F)
Before cycling	2.6	3.3	9.0	1.3×10^{-3}
After cycling	3.5	9.7	24.8	1.6×10^{-3}

Table 1. Fitting EIS parameters obtained from the LIC cell before and after 5000 cycles.

the increased contact resistance between active materials and current collector[64]. The capacitive component in the equivalent circuit is substituted with CPE because of the porous nature of both AC and CNF@CoNi$_2$S$_4$ electrodes. Warburg impedance W1 is associated with the diffusion of lithium ions through the network of CNF@CoNi$_2$S$_4$ anode. Summarized fitting parameters estimated for the LIC2.6 are shown in the Table 1.

In order to demonstrate the practical applicability of the LIC, we charged LIC2.6 at contact potential of 3 V for less than 60 s and discharged through 18 LEDs making KU (initials of Kettering University) which lasts for 2 min as shown in the Fig. 6c. This indicates its potential application in future appliances.

Conclusions

In summary, we have fabricated a novel LIC based on CNF supported CoNi$_2$S$_4$ nanoparticles anode and AC cathode in Li ions containing nonaqueous electrolyte in order to bridge the gap between LIB and supercapacitor. The CNF webs decorated with CoNi$_2$S$_4$ nanoparticles offer highly porous structure which reduces pathways for the electrolytic diffusion, while, the good conducting behavior of both CoNi$_2$S$_4$ and CNF acts as an expressway for electronic diffusion for efficient electrochemical reactions at the electrode/electrolyte interface. The capacitive or the surface controlled contribution of CNF@CoNi$_2$S$_4$ electrode was found to be 73% which demonstrates excellent rate capability and ensures its ability to be used for LIC. LIC2.6 fabricated with CNF@CoNi$_2$S$_4$ to AC mass ratio of 1:2.6 showed excellent energy density of 85.4 Wh kg^{-1} with the power density of 150 W kg^{-1}. Also, even at the huge power density of 15 kW kg^{-1}, LIC2.6 can supply the energy density of 35 Wh kg^{-1}. Therefore, it is worth mentioning that the CNF@CoNi$_2$S$_4$ electrode is an excellent anode material for the fabrication of high performance LICs to be used for electric and plugged in electric vehicles.

Methods

Chemicals. Cobalt chloride (CoCl$_2$·6H$_2$O) and nickel chloride (NiCl$_2$·6H$_2$O) were purchased from Alfa Aesar. Polyacrylonitrile (PAN, Mw = 150,000) and Thiourea were purchased from Sigma-Aldrich.

Synthesis of CNF@CoNi$_2$S$_4$ hybrid anode. At first carbon nanofibers were fabricated via electrospinning method. Briefly, homogeneous solution of 12% PAN in DMF was prepared and filled into a syringe with a needle having an inner diameter of 0.64 mm. The electrospinning process was done at an applied voltage of 14 kV with a feeding speed of 1 mL h^{-1} and the distance between the tip of the needle and the collector was 20 cm. As prepared PAN fibers were pre-oxidized at 280 °C for 2 h with a heating rate of 1 °C min^{-1}. Furthermore, pre-oxidized fibers were employed for carbonization process at 950 °C for 0.5 h with a heating rate of 3 °C min^{-1} under Ar atmosphere. After carbonization, CNF mats were cut into suitable pieces and employed as a substrate for electrodeposition process. Prior to deposition, CNF mats were first electrochemically treated in 1 M H$_2$SO$_4$ solution using cyclic voltammetry within the potential window of −0.7 to +1.2 V vs. Ag/AgCl at the scan rate of 50 mV s^{-1} for 100 cycles. Co-Ni sulfide was coated on the CNF mats using potentiodynamic electrodeposition method within a potential window of +0.2 to −1.2 V vs. Ag/AgCl at the scan rate of 5 mV s^{-1} for 25 cycles. An electrochemical cell was assembled in a three-electrode configuration in which Cu supported CNF mat, Pt and Ag/AgCl were used as working, counter and reference electrodes, respectively. The electrodeposition bath was formed of 5 mM CoCl$_2$·6H$_2$O, 10 mM NiCl$_2$·6H$_2$O and 0.75 M thiourea in 50 ml deionized (DI) water. After

deposition, electrodes were thoroughly rinsed with DI water and dried at room temperature. In order to improve the crystallinity of the sample, dried electrodes were further heat treated at 300 °C for 2 h with a heating rate of 5 °C min⁻¹ under Ar atmosphere. These electrodes were punched into circular discs and weighted via micro-balance with an accuracy of 0.01 mg.

Material characterization.   The morphology of the sample was characterized by environmental scanning electron microscope, E-SEM, (Quanta 200 s, Phillips Electron Optics Company) and transmission electron microscope, TEM, (JEOL JEM-2100, USA). X-ray diffraction, XRD pattern was collected using a diffractometer (Rigaku SmartLab) equipped with a Cu Kα radiation source ($\lambda = 1.5406$ A). The electronic states of the different elements in the sample were examined using X-ray photoelectron spectroscopy, XPS, (Kratos Axis Ultra).

Electrochemical measurement.   All electrochemical measurements were performed at room temperature. The galvanostatic charge-discharge was performed on a LAND-CT2001A battery testing system. The cyclic voltammetry (CV) and electrochemical impedance spectroscopy (EIS) measurements were made through Biologic SP-300 potentiostat. Electrochemical performance of the CNF@CoNi$_2$S$_4$ electrode was evaluated in half coin cells (CR2032) assembled in an Ar-filled glove box. Lithium metal was used as a counter and reference electrode and Celgard membrane was used as a separator. The electrolyte was prepared by dissolving 1 M LiPF$_6$ in the mixture of ethylene carbonate (EC) and diethyl carbonate (DEC) with a volume ratio of 1:2. The LICs such as LIC0.25, LIC0.4, LIC0.9, LIC1.6, LIC2.9, LIC2.6 and LIC4.3 were formed of CNF@CoNi$_2$S$_4$ electrode masses as 4.4, 3.9, 3.2, 2.9, 1.7, 1.4 and 1.5 mg cm⁻², and the electrode densities are 0.09, 0.08, 0.06, 0.06, 0.03, 0.03 and 0.03 g cm⁻³ respectively. Also, LIC was fabricated with prelithiated CNF@CoNi$_2$S$_4$ as anode, AC as a cathode and Celgard membrane as a separator. Prelithiation of the CNF@CoNi$_2$S$_4$ was performed by making direct contact of Li metal with one or two drops of electrolyte in between for 3h[48,65]. AC cathode was fabricated by mixing AC powder, acetylene black and polyvinylidene fluoride (PVDF) in N-methyl-2-pyrrolidine (NMP) solvent with a mass ratio of 80:10:10 and the slurry was coated on the Al foil. Further, the electrodes were dried at 120 °C for 8 h. The energy and power density of the LIC were calculated using following formulae,

$$P = I \times \Delta V/m \tag{8}$$

$$E = P \times t/3600 \tag{9}$$

$$\Delta V = V_{max} - V_{min} \tag{10}$$

Where, I is the discharge current (A), t is the discharge time (s), m is the total active material on both electrodes (kg) and V_{max} and V_{min} are the upper and lower potentials during charge-discharge process.

Data Availability.   The datasets generated during the current study are available from the corresponding author on reasonable request.

References

1. Wu, Z., Li, L., Yan, J. M. & Zhang, X. B. Materials design and system construction for conventional and new-concept supercapacitors. *Adv. Sci.* **4**, 1600382 (2017).
2. Zhang, S. *et al.* High performance lithium-ion hybrid capacitors employing Fe$_3$O$_4$-graphene composite anode and activated carbon cathode. *ACS Appl. Mater. Interfaces* **9**, 17136–17144 (2017).
3. Amatucci, G. G., Badway, F., Du Pasquier, A. & Zheng, T. An asymmetric hybrid nonaqueous energy storage cell. *J. Electrochem. Soc.* **148**, A930–A939, https://doi.org/10.1149/1.1383553 (2001).
4. Jung, H.-G., Venugopal, N., Scrosati, B. & Sun, Y.-K. A high energy and power density hybrid supercapacitor based on an advanced carbon-coated Li$_4$Ti$_5$O$_{12}$ electrode. *J. Power Sources* **221**, 266–271, https://doi.org/10.1016/j.jpowsour.2012.08.039 (2013).
5. Khomenko, V., Raymundo-Piñero, E. & Béguin, F. High-energy density graphite/AC capacitor in organic electrolyte. *J. Power Sources* **177**, 643–651, https://doi.org/10.1016/j.jpowsour.2007.11.101 (2008).
6. Du, H. *et al.* Graphdiyne applied for lithium-ion capacitors displaying high power and energy densities. *Nano Energy* **22**, 615–622, https://doi.org/10.1016/j.nanoen.2016.02.052 (2016).
7. Saito, M., Takahashi, K., Ueno, K. & Seki, S. Electrochemical charge/discharge properties of Li pre-doped Si nanoparticles for use in hybrid capacitor systems. *J. Electrochem. Soc.* **163**, A3140–A3145, https://doi.org/10.1149/2.1361614jes (2016).
8. Ulaganathan, M., Aravindan, V., Ling, W. C., Yan, Q. & Madhavi, S. High energy Li-ion capacitors with conversion type Mn$_3$O$_4$ particulates anchored to few layer graphene as the negative electrode. *J. Mater. Chem. A* **4**, 15134–15139, https://doi.org/10.1039/c6ta05944a (2016).
9. Wang, F. *et al.* A quasi-solid-state Li-ion capacitor based on porous TiO$_2$ hollow microspheres wrapped with graphene nanosheets. *Small* **12**, 6207–6213, https://doi.org/10.1002/smll.201602331 (2016).
10. Ma, Y., Chang, H., Zhang, M. & Chen, Y. Graphene-based materials for lithium-ion hybrid supercapacitors. *Adv. Mater.* **27**, 5296–5308, https://doi.org/10.1002/adma.201501622 (2015).
11. Peng, C.-J., Tsai, D.-S., Chang, C.-H. & Wei, H.-Y. The lithium ion capacitor with a negative electrode of lithium titanium zirconium phosphate. *J. Power Sources* **274**, 15–21, https://doi.org/10.1016/j.jpowsour.2014.10.047 (2015).
12. Lim, Y.-G. *et al.* Incorporation of conductive polymer into soft carbon electrodes for lithium ion capacitors. *J. Power Sources* **299**, 49–56, https://doi.org/10.1016/j.jpowsour.2015.08.083 (2015).
13. Liu, M. *et al.* Controllable formation of niobium nitride/nitrogen-doped graphene nanocomposites as anode materials for lithium-ion capacitors. *Part. Part. Syst. Char.* **32**, 1006–1011, https://doi.org/10.1002/ppsc.201500095 (2015).
14. Kaliyappan, K., Amaresh, S. & Lee, Y. S. LiMnBO$_3$ nanobeads as an innovative anode material for high power lithium ion capacitor applications. *ACS Appl. Mater. Interfaces* **6**, 11357–11367, https://doi.org/10.1021/am5019034 (2014).
15. Qu, W.-H. *et al.* Combination of a SnO$_2$–C hybrid anode and a tubular mesoporous carbon cathode in a high energy density non-aqueous lithium ion capacitor: preparation and characterisation. *J. Mater. Chem. A* **2**, 6549–6557, https://doi.org/10.1039/c4ta00670d (2014).
16. Sun, X. *et al.* High performance lithium-ion hybrid capacitors with pre-lithiated hard carbon anodes and bifunctional cathode electrodes. *J. Power Sources* **270**, 318–325, https://doi.org/10.1016/j.jpowsour.2014.07.146 (2014).

17. Wang, L. P. *et al.* High-performance hybrid electrochemical capacitor with binder-free Nb₂O₅@graphene. *RSC Adv.* **4**, 37389–37394, https://doi.org/10.1039/c4ra06674j (2014).

18. Aravindan, V., Shubha, N., Ling, W. C. & Madhavi, S. Constructing high energy density non-aqueous Li-ion capacitors using monoclinic TiO₂-B nanorods as insertion host. *J. Mater. Chem. A* **1**, 6145–6151, https://doi.org/10.1039/c3ta11103b (2013).

19. Byeon, A. *et al.* Lithium-ion capacitors with 2D Nb₂CTₓ (MXene) – carbon nanotube electrodes. *J. Power Sources* **326**, 686–694, https://doi.org/10.1016/j.jpowsour.2016.03.066 (2016).

20. Fan, Q., Yang, M., Meng, Q., Cao, B. & Yu, Y. Activated-nitrogen-doped graphene-based aerogel composites as cathode materials for high energy density lithium-ion supercapacitor. *J. Electrochem. Soc.* **163**, A1736–A1742, https://doi.org/10.1149/2.1271608jes (2016).

21. Rauhala, T., Leis, J., Kallio, T. & Vuorilehto, K. Lithium-ion capacitors using carbide-derived carbon as the positive electrode – A comparison of cells with graphite and Li₄Ti₅O₁₂ as the negative electrode. *J. Power Sources* **331**, 156–166, https://doi.org/10.1016/j.jpowsour.2016.09.010 (2016).

22. Zhang, F. *et al.* Uniform incorporation of flocculent molybdenum disulfide nanostructure into three-dimensional porous graphene as an anode for high-performance lithium ion batteries and hybrid supercapacitors. *ACS Appl. Mater. Interfaces* **8**, 4691–4699, https://doi.org/10.1021/acsami.5b11705 (2016).

23. Amaresh, S., Karthikeyan, K., Jang, I.-C. & Lee, Y. Single-step microwave mediated synthesis of the CoS₂ anode material for high rate hybrid supercapacitors. *J. Mater. Chem. A* **2**, 11099–11106 (2014).

24. Feng, C., Huang, L., Guo, Z. & Liu, H. Synthesis of tungsten disulfide (WS₂) nanoflakes for lithium ion battery application. *Electrochem. Commun.* **9**, 119–122, https://doi.org/10.1016/j.elecom.2006.08.048 (2007).

25. Hu, L., Ren, Y., Yang, H. & Xu, Q. Fabrication of 3D hierarchical MoS₂/polyaniline and MoS₂/C architectures for lithium-ion battery applications. *ACS Appl. Mater. Interfaces* **6**, 14644–14652, https://doi.org/10.1021/am503995s (2014).

26. Lai, C.-H. *et al.* Direct growth of high-rate capability and high capacity copper sulfide nanowire array cathodes for lithium-ion batteries. *J. Mater. Chem.* **20**, 6638–6645, https://doi.org/10.1039/c0jm00434k (2010).

27. Mahmood, N., Zhang, C. & Hou, Y. Nickel sulfide/nitrogen-doped graphene composites: phase-controlled synthesis and high performance anode materials for lithium ion batteries. *Small* **9**, 1321–1328, https://doi.org/10.1002/smll.201203032 (2013).

28. Seo, J.-W. *et al.* Two-dimensional SnS₂ nanoplates with extraordinary high discharge capacity for lithium ion batteries. *Adv. Mater.* **20**, 4269–4273, https://doi.org/10.1002/adma.200703122 (2008).

29. Wu, R. *et al. In-situ* formation of hollow hybrids composed of cobalt sulfides embedded within porous carbon polyhedra/carbon nanotubes for high-performance lithium-ion batteries. *Adv. Mater.* **27**, 3038–3044, https://doi.org/10.1002/adma.201500783 (2015).

30. Zhang, Z. *et al.* Synthesis of bismuth sulfide/reduced graphene oxide composites and their electrochemical properties for lithium ion batteries. *Electrochim. Acta* **114**, 88–94, https://doi.org/10.1016/j.electacta.2013.09.174 (2013).

31. Zou, R. *et al.* Three-dimensional-networked NiCo₂S₄ nanosheet array/carbon cloth anodes for high-performance lithium-ion batteries. *NPG Asia Mater.* **7**, e195, https://doi.org/10.1038/am.2015.63 (2015).

32. Sun, G., Sun, L., Xie, H. & Liu, J. Electrospinning of nanofibers for energy applications. *Nanomaterials* **6**, 129 (2016).

33. Ghouri, Z. K., Barakat, N. A. & Kim, H. Y. Influence of copper content on the electrocatalytic activity toward methanol oxidation of CoχCuy alloy nanoparticles-decorated CNFs. *Sci. Rep.* **5**, 16695 (2015).

34. Li, B. *et al.* Co₃O₄ nanoparticles decorated carbon nanofiber mat as binder-free air-cathode for high performance rechargeable zinc-air batteries. *Nanoscale* **7**, 1830–1838, https://doi.org/10.1039/c4nr05988c (2015).

35. Shen, Z. *et al.* Tin nanoparticle-loaded porous carbon nanofiber composite anodes for high current lithium-ion batteries. *J. Power Sources* **278**, 660–667, https://doi.org/10.1016/j.jpowsour.2014.12.106 (2015).

36. Shen, J. *et al.* CoNi₂S₄-graphene-2D-MoSe₂ as an advanced electrode material for supercapacitors. *Adv. Energy Mater.* **6**, 1600341, https://doi.org/10.1002/aenm.201600341 (2016).

37. Hu, W. *et al.* CoNi₂S₄ nanosheet arrays supported on nickel foams with ultrahigh capacitance for aqueous asymmetric supercapacitor applications. *ACS Appl. Mater. Interface* **6**, 19318–19326, https://doi.org/10.1021/am5053784 (2014).

38. He, W. *et al.* Ultrathin and porous Ni₃S₂/CoNi₂S₄ 3D-network structure for superhigh energy density asymmetric supercapacitors. *Adv. Energy Mater.*, 1700983, https://doi.org/10.1002/aenm.201700983 (2017).

39. Yang, J. *et al.* Electroactive edge site-enriched nickel–cobalt sulfide into graphene frameworks for high-performance asymmetric supercapacitors. *Energy Environ. Sci.* **9**, 1299–1307, https://doi.org/10.1039/c5ee03633j (2016).

40. Chen, H. *et al.* Electrospun carbon nanofibers coated with urchin-like ZnCo₂O₄ nanosheets as a flexible electrode material. *J. Mater. Chem. A* **4**, 5958–5964, https://doi.org/10.1039/c6ta01880g (2016).

41. Yu, D. J. *et al.* Nickel cobalt sulfide nanotube array on nickel foam as anode material for advanced lithium-ion batteries. *Electrochim. Acta* **198**, 280–286, https://doi.org/10.1016/j.electacta.2016.01.189 (2016).

42. Wang, R. *et al.* Heat-induced formation of porous and free-standing MoS₂/GS hybrid electrodes for binder-free and ultralong-life lithium ion batteries. *Nano Energy* **8**, 183–195, https://doi.org/10.1016/j.nanoen.2014.05.009 (2014).

43. Jin, R., Liu, D., Liu, C. & Liu, G. Hierarchical NiCo₂S₄ hollow spheres as a high performance anode for lithium ion batteries. *RSC Adv.* **5**, 84711–84717 (2015).

44. Kumar, V. *et al.* Design of mixed-metal silver decamolybdate nanostructures for high specific energies at high power density. *Adv. Mater.* **28**, 6966–6975 (2016).

45. Augustyn, V. *et al.* B. High-rate electrochemical energy storage through Li+ intercalation pseudocapacitance. *Nat. Mater.* **12**, 518–522 (2013).

46. Ardizzone, S., Fregonara, G. & Trasatti, S. "Inner" and "outer" active surface of RuO₂ electrodes. *Electrochim. Acta* **35**, 263–267 (1990).

47. Wang, H. *et al.* A high-energy lithium-ion capacitor by integration of a 3D interconnected titanium carbide nanoparticle chain anode with a pyridine-derived porous nitrogen-doped carbon cathode. *Adv. Funct. Mater.* **26**, 3082–3093, https://doi.org/10.1002/adfm.201505240 (2016).

48. Li, S. *et al.* A high-performance lithium-ion capacitor based on 2D nanosheet materials. *Small* **13**, 1602893 (2017).

49. Yang, W. *et al.* One-step growth of 3D CoNi₂S₄ nanorods and cross-linked NiCo₂S₄ nanosheet arrays on carbon paper as anodes for high-performance lithium ion batteries. *Chem. Commun.* **52**, 5258–5261 (2016).

50. Wu, H. *et al.* Stable Li-ion battery anodes by *in-situ* polymerization of conducting hydrogel to conformally coat silicon nanoparticles. *Nat. Commun.* **4**, 1943, https://doi.org/10.1038/ncomms2941 (2013).

51. Jeżowski, P., Fic, K., Crosnier, O., Brousse, T. & Béguin, F. Lithium rhenium(vii) oxide as a novel material for graphite pre-lithiation in high performance lithium-ion capacitors. *J. Mater. Chem. A* **4**, 12609–12615, https://doi.org/10.1039/c6ta03810g (2016).

52. Suryawanshi, A. *et al.* A comparative evaluation of differently synthesized high surface area carbons for Li-ion hybrid electrochemical supercapacitor application: Pore size distribution holds the key. *Appl. Mater. Today* **2**, 1–6, https://doi.org/10.1016/j.apmt.2015.11.002 (2016).

53. Wang, J., Li, H., Shen, L., Dong, S. & Zhang, X. Nb₂O₅ nanoparticles encapsulated in ordered mesoporous carbon matrix as advanced anode materials for Li ion capacitors. *RSC Adv.* **6**, 71338–71344, https://doi.org/10.1039/c6ra11460a (2016).

54. Yuvaraj, S., Karthikeyan, K., Kalpana, D., Lee, Y. S. & Selvan, R. K. Surfactant-free hydrothermal synthesis of hierarchically structured spherical CuBi₂O₄ as negative electrodes for Li-ion hybrid capacitors. *J. Colloid Interface Sci.* **469**, 47–56, https://doi.org/10.1016/j.jcis.2016.01.060 (2016).

55. Sun, X. *et al*. Electrochemical performances and capacity fading behaviors of activated carbon/hard carbon lithium ion capacitor. *Electrochim. Acta* **235**, 158–166, https://doi.org/10.1016/j.electacta.2017.03.110 (2017).
56. Yu, X. *et al*. A high-power lithium-ion hybrid electrochemical capacitor based on citrate-derived electrodes. *Electrochim. Acta* **228**, 76–81, https://doi.org/10.1016/j.electacta.2017.01.058 (2017).
57. Arunkumar, P. *et al*. Nb$_2$O$_5$/graphene nanocomposites for electrochemical energy storage. *RSC Adv.* **5**, 59997–60004, https://doi.org/10.1039/c5ra07895d (2015).
58. Liu, Y., Zhang, D., Shang, Y., Liu, Y. & Zhang, J. Synthesis of nitrogen-doped graphene as highly effective cathode materials for Li-ion hybrid supercapacitors. *J. Electrochem. Soc.* **162**, A2123–A2130, https://doi.org/10.1149/2.0721510jes (2015).
59. Shi, Z., Zhang, J., Wang, J., Shi, J. & Wang, C. Effect of the capacity design of activated carbon cathode on the electrochemical performance of lithium-ion capacitors. *Electrochim. Acta* **153**, 476–483, https://doi.org/10.1016/j.electacta.2014.12.018 (2015).
60. Ye, L. *et al*. A high performance Li-ion capacitor constructed with Li$_4$Ti$_5$O$_{12}$/C hybrid and porous graphene macroform. *J. Power Sources* **282**, 174–178, https://doi.org/10.1016/j.jpowsour.2015.02.028 (2015).
61. Cai, Y., Zhao, B., Wang, J. & Shao, Z. Non-aqueous hybrid supercapacitors fabricated with mesoporous TiO$_2$ microspheres and activated carbon electrodes with superior performance. *J. Power Sources* **253**, 80–89, https://doi.org/10.1016/j.jpowsour.2013.11.097 (2014).
62. Feng, L. *et al*. MnO$_2$ prepared by hydrothermal method and electrochemical performance as anode for lithium-ion battery. *Nanoscale Res. Lett.* **9**, 290, https://doi.org/10.1186/1556-276X-9-290 (2014).
63. Yang, L. *et al*. Lithium compound deposition on mesocarbon microbead anode of lithium ion batteries after long-term cycling. *ACS Appl. Mater. Interfaces* **6**, 12962–12970, https://doi.org/10.1021/am502887v (2014).
64. Li, Y., Yu, S., Zhao, D., Li, X.-M. & He, T. Effect of different reduction methods on electrochemical cycling stability of reduced graphene oxide in supercapacitors. *J. Appl. Electrochem.* **45**, 57–65, https://doi.org/10.1007/s10800-014-0771-2 (2014).
65. Kim, M. *et al*. A fast and efficient pre-doping approach to high energy density lithium-ion hybrid capacitors. *J. Mater. Chem. A* **2**, 10029–10033, https://doi.org/10.1039/C4TA00678J (2014).

Acknowledgements

Author Contributions

A.D.J. performed the experiments. S.Y. performed and analyzed the X.P.S. data. A.D.J. wrote the manuscript. A.D.J. and X.Z. designed the experiments. D.B. helped apparatus set up and PVP carbon nanofibers manufacturing. X.Z. supervised the research. All authors reviewed the manuscript.

Additional Information

Supplementary information accompanies this paper at https://doi.org/10.1038/s41598-018-19787-z.

Competing Interests: The authors declare that they have no competing interests.

Publisher's note: Springer Nature remains neutral with regard to jurisdictional claims in published maps and institutional affiliations.